Factors Shaping the Confocal Image of the Calcium Spark in Cardiac Muscle Cells

Victor R. Pratusevich and C. William Balke
Department of Physiology and Department of Medicine, Division of Cardiology, University of Maryland School of Medicine, Baltimore, Maryland 21201 USA

ABSTRACT The interpretation of confocal line-scan images of local $[Ca^{2+}]_i$ transients (such as Ca^{2+} sparks in cardiac muscle) is complicated by uncertainties in the position of the origin of the Ca^{2+} spark (relative to the scan line) and by the dynamics of Ca^{2+}–dye interactions. An investigation of the effects of these complications modeled the release, diffusion, binding, and uptake of Ca^{2+} in cardiac cells (producing a theoretical Ca^{2+} spark) and image formation in a confocal microscope (after measurement of its point-spread function) and simulated line-scan images of a theoretical Ca^{2+} spark (when it was viewed from all possible positions relative to the scan line). In line-scan images, Ca^{2+} sparks that arose in a different optical section or with the site of origin displaced laterally from the scan line appeared attenuated, whereas their rise times slowed down only slightly. These results indicate that even if all Ca^{2+} sparks are perfectly identical events, except for their site of origin, there will be an apparent variation in the amplitude and other characteristics of Ca^{2+} sparks as measured from confocal line-scan images. The frequency distributions of the kinetic parameters (i.e., peak amplitude, rise time, fall time) of Ca^{2+} sparks were calculated for repetitive registration of stereotyped Ca^{2+} sparks in two experimental situations: 1) random position of the scan line relative to possible SR Ca^{2+}-release sites and 2) fixed position of the scan line going through a set of possible SR Ca^{2+}-release sites. The effects of noise were incorporated into the model, and a visibility function was proposed to account for the subjective factors that may be involved in the evaluation of Ca^{2+}-spark image parameters from noisy experimental recordings. The mean value of the resulting amplitude distributions underestimates the brightness of in-focus Ca^{2+} sparks because large numbers of out-of-focus Ca^{2+} sparks are detected (as small Ca^{2+} sparks). The distribution of peak amplitudes may split into more than one subpopulation even when one is viewing stereotyped Ca^{2+} sparks because of the discrete locations of possible SR Ca^{2+}-release sites in mammalian ventricular heart cells.

INTRODUCTION

Spatially localized, subcellular changes in calcium-ion concentration ($[Ca^{2+}]_i$), such as calcium "puffs" (Parker and Yao, 1991), "blips" (Parker and Yao, 1996), "Ca^{2+} sparks" (Cheng et al., 1993; Cannell et al., 1994, 1995; Niggli and Lipp, 1995), and local $[Ca^{2+}]_i$ transients (López-López et al., 1994, 1995; Shacklock et al., 1995) are typically studied with laser scanning confocal microscopy and fluorescent Ca^{2+} indicators (fluo-3). To achieve adequate temporal resolution, line-scan confocal images have been used to characterize the spatiotemporal properties of Ca^{2+} sparks in skeletal (Tsugorka et al., 1995; Klein et al., 1996) and cardiac (López-López et al., 1995; Cannell et al., 1995; Berlin, 1995; Cheng et al., 1996) muscle cells. Despite the improved spatial resolution of the confocal microscope, the interpretation of confocal line-scan images of $[Ca^{2+}]_i$ is difficult because 1) there is still some contribution of out-of-focus fluorescence, 2) Ca^{2+} may diffuse from sites where it is released into the volume being observed, and 3) the spatiotemporal profile of $[Ca^{2+}]_i$ is different from that of the dye fluorescence signal as a result of the limited dynamic range and reaction speed of the indicator dye. To quantify correctly the spatiotemporal properties of local $[Ca^{2+}]_i$ transients it is important to understand fully the characteristics of image formation in the confocal microscope, the factors that govern the diffusion of Ca^{2+}, and the characteristics of the Ca^{2+} indicator. Here we will be concerned principally with line-scan images of Ca^{2+} sparks in mammalian cardiac muscle. We developed a theoretical model that combines simulation of the release, diffusion, binding, and uptake of Ca^{2+} with simulation of image formation in our particular confocal microscope. The model was then used to compute theoretical line-scan images of an idealized Ca^{2+} spark. The effects of noise were incorporated into the model, and a visibility function was proposed to account for the subjective factors that may be involved in the evaluation of Ca^{2+}-spark image parameters from noisy experimental recordings. For two common experimental situations, specific predictions were made as to the relation of experimentally measured image parameters to the actual profile of $[Ca^{2+}]_i$ in the cell.

Received for publication 2 April 1996 and in final form 12 September 1996.

Address reprint requests to C. William Balke, M.D., University of Maryland School of Medicine, Department of Physiology, Howard Hall, Room 560, 660 West Redwood Street, Baltimore, MD 21201-1595. Tel.: 410-328-8789; Fax: 410-328-2062; E-mail: bbalke@heart.ab.umd.edu.

0006-3495/96/12/2942/16 $2.00

METHODS

Overview of model

The model is presented schematically in Fig. 1. A major component is the system of partial differential equations (Fig. 1; *step 1*) that describes the diffusion, binding, and sequestration of Ca^{2+} within the cytoplasm of a mammalian cardiac cell. To obtain particular solutions (viz., spatially resolved $[Ca^{2+}]_i$ and fluorescence transients) to this system of equations we first converted the partial differential equations into ordinary differen

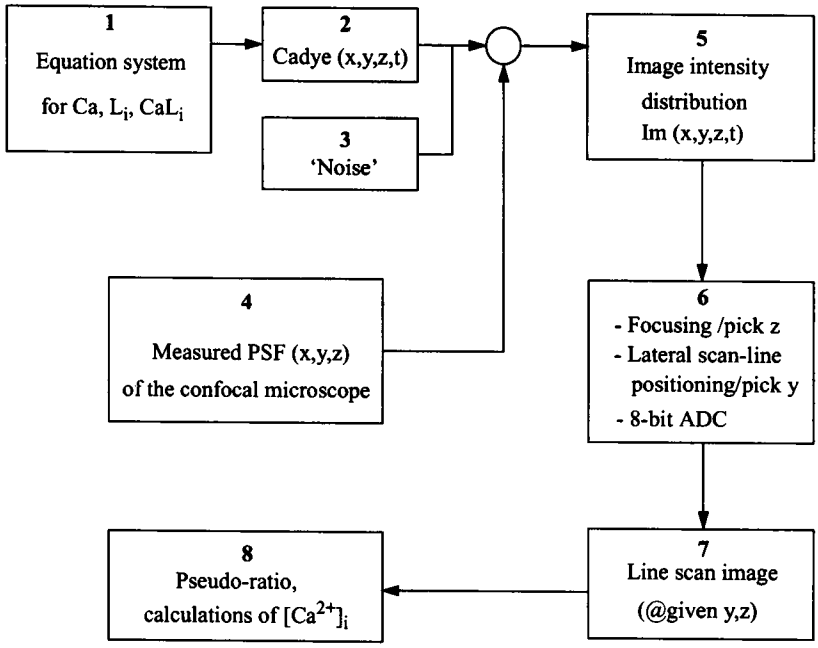

FIGURE 1 Overview of the model. Schematic representation of the major steps in the simulation of the line-scan confocal imaging of the Ca^{2+} spark. A system (*1*) of model equations for Ca^{2+} release, diffusion, binding, and sequestration was numerically solved. (Here variables L_i, $i = 1, 2...$ represent the concentration of fluo-3 or the other intracellular buffer; CaL_i denotes the concentration of the bound form of Ca^{2+}.) The computed spatial distribution of bound Ca^{2+} to fluo-3 (Cadye, *2*) was convolved in the 3-D space, at each moment of time, with the measured PSF (*4*) of the confocal imaging system, to arrive at the distribution of the spatiotemporal image intensity (Im, *5*). Then the line-scan images were simulated for particular y, z locations of the scan line (*6-8*). In some simulations a term describing noise (*3*) was added to the theoretical Cadye distribution. The direction of the scan line, x, was assumed to be parallel to long axis of a cardiac cell; z is the direction of optical axis of the microscope, and y is normal to the x, z plane (see Fig. 3).

tial equations by spatial discretization of the simulation space, which consisted of a small, representative part of the entire cardiac cell (see the next section). Each voxel of this space is then considered spatially homogeneous. The entire system of simultaneous ordinary differential equations, consisting of the equations that describe diffusion, binding, and sequestration of Ca^{2+} in each voxel, can then be solved by computerized numerical methods. (The specific equations are given below.) As indicated above, the solution to this system of equations includes the variation in free $[Ca^{2+}]_i$ as a function of time and space (the spatiotemporal $[Ca^{2+}]_i$ transient) and the variation in the concentration of Ca-fluo-3 (Fig. 1; *step 2*) (the spatiotemporal fluo-3-transient) to which fluorescence is directly proportional. The probabilistic nature of the fluorescence signal produces variability that can be characterized as noise (Fig. 1; *step 3*). Fluorescence light (photons) arising from Ca-fluo-3 is captured by the objective lens of the microscope, propagates through the confocal microscope, and is ultimately converted into an electrical signal by a photomultiplier tube. At any point in time three-dimensional convolution of fluorescence with the point-spread function (PSF) (Fig. 1; *step 4*) of the microscope produces a theoretical three-dimensional confocal image (Fig. 1; *step 5*) of Ca^{2+}-dependent fluorescence. Theoretical line-scan images along the x axis (Fig. 1; *step 7*) are produced by choice of a line through this volume (i.e., choice of a value of z and y) and by simulation of the digitization of the fluorescence intensity with an 8-bit analog-to-digital converter (Fig. 1; *step 6*), as is used in our confocal microscope. These fluorescence images are then used to compute Ca^{2+} images (Fig. 1; *step 8*).

A specialized high-level programming language designed for computation of finitedifference approximations to diffusion-reaction problems, FACSIMILE (AEA Technologies, Harwell, UK), was used to solve the system of ordinary differential equations. Computations and image analysis were performed with the software, IDL (Research Systems, Inc., Boulder, CO), on an IBM Risc System/6000 workstation (IBM Corp., Armonk, NY).

Optical properties: point-spread function

As described above, it was necessary to characterize the optical transfer function of the confocal microscope. The microscope is a Nikon Diaphot TMD inverted microscope (Nikon Inc., Melville, NY) to which a Bio-Rad MRC-600 confocal imaging system is attached (Bio-Rad, Microscience Division, Hemel Hempstead, UK). The objective lens is a planar-apochromat oil-immersion lens of magnification 60× and numerical aperture 1.4 (Nikon Inc.). The microscope objective can be moved in the z axis in steps of 0.02 μm through the use of a custom-made piezoelectric device and a microcomputer controller.

It has been shown by others (Keating and Cork, 1994; Hiraoka et al., 1990; Blumenfeld, 1992; Agard et al, 1989) that the shape of the PSF is an important factor in determining the properties of images and that theoretical PSFs do not represent adequately the inherent optical distortion in most experimental situations. Therefore, the actual PSF for the experimental setup should be measured to analyze correctly the underlying image-formation process. Hence we measured the PSF of our confocal microscope (Fig. 2) experimentally with the setup described above by imaging a fluorescent bead, 0.1 μm in diameter, that had been phagocytized by an alveolar macrophage (Gasbjerg et al., 1994). (This immobilized the bead in the cytoplasm and provided a medium with a refractive index appropriate for recordings from living cells.) To permit three-dimensional (3-D) reconstruction of the PSF, 16 optical sections of the bead were taken at 0.28-μm intervals along the z axis. As in experiments on cardiac cells loaded with fluo-3, the adjustable confocal pinhole aperture was set at four small divisions (pinhole diameter 2.5 mm), providing the trade-off between the axial resolution and the signal collection (Sandison et al., 1995). Fig. 2 shows the measured 3-D PSF (*upper panel*) and the radial isolevel contour map and axial distribution of the z dependence for image intensity (*bottom panel*). Notably, the measured PSF is highly asymmetric. The half-maximum width of the measured PSF was 0.48 μm in the y dimension and 1.30 μm along the z dimension. These data are close to those reported elsewhere for the confocal microscope (Shaw, 1995) and, as expected, are consistently smaller than those for conventional epifluorescence microscopes (Agard et al., 1989; Blumenfeld et al., 1992).

Geometry of the simulated cellular volume

The entire volume in which simulation was performed was 11.92 μm × 2.97 μm × 8.64 μm (in the x, y, and z directions, respectively). The dimensions of a voxel were 0.271 μm in x and 0.135 μm in y and z. These dimensions were convenient because the pixels of our actual line-scan confocal images are also 0.271 μm in x and because the voxels of the actual PSF (see below) are integral fractions of 0.271, that is, 0.068 μm (x) by 0.068 μm (y) by 0.271 μm (z). The simulation volume was 6.5 sarcomeres long (x), ~6 sarcomeres wide (y), and 17 sarcomeres deep (z). In theory,

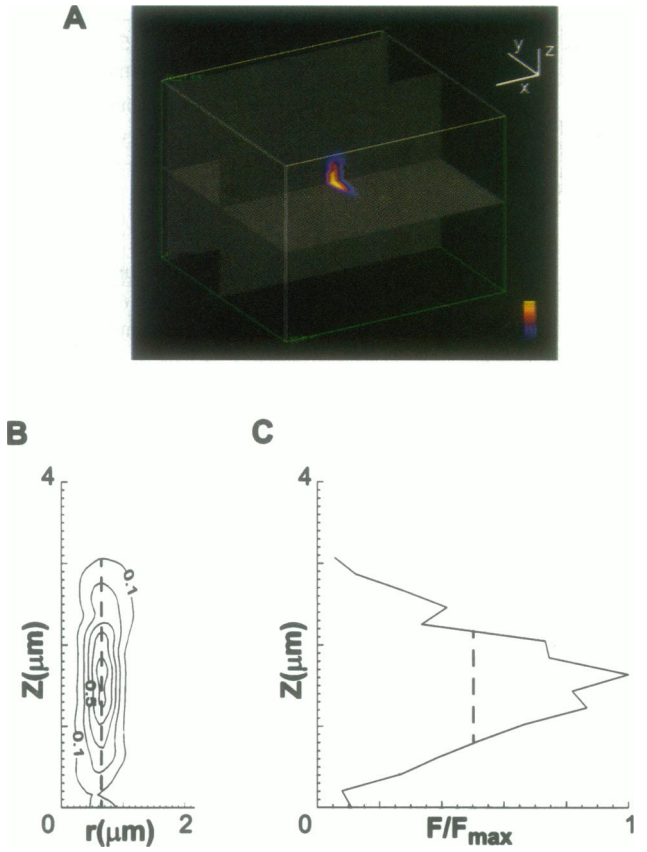

FIGURE 2 PSF of the confocal microscope. (*Top*) The PSF of our confocal imaging system. As a reference, the large cuboid outlines the simulation space (same as in Fig. 3). Calibration bars: $x = 2.16$ μm, $y = 0.68$ μm, $z = 1.35$ μm. The color scale covers the range of relative fluorescence intensities, F/F_{max}, from 0 to 1. (*Bottom, left*) Isolevel contours of the PSF, averaged between two orthogonal, through-axis sections, and smoothed (width, 3 pixels). The dashed line shows the z-axis position. The abscissa (radial coordinate) and the ordinate (axial coordinate) are given in micrometers. Note that the apparent distortion of the x-versus-y direction is due primarily to a difference in the display scales. Levels of maximal intensity are 10%, 30%, 50%, 70%, and 90%. (*Bottom, right*) Axial variation of the PSF at the central (x, y) position. The dashed line shows the width at half-maximum level. Abscissa, intensity normalized to maximum. Ordinate, axial coordinate, in micrometers.

the PSF and the Ca^{2+} image are space functions that expand indefinitely. However, the practical choice for the simulation volume was based on the minimum value that was large enough that both the PSF and the Ca^{2+} image could decay to values well below a fraction of a percent of their respective maximum levels at the borders of the simulation space.

To model the spatially localized release and uptake of Ca^{2+} it was necessary to specify the location and the function of the sarcoplasmic reticulum (SR) and the transverse tubules (t-tubules) throughout the simulation volume. In general, the SR (blue elements in Fig. 3 *A*) is modeled as two sets of parallel planes, 0.675 μm apart, one of which is normal to the z axis (xy planes) and the other of which is normal to the y axis (xz planes). Special techniques, described below, were used to simulate the reticular nature of the SR. t-Tubules are represented by a stack of elements (colored magenta in Fig. 3 *A*) parallel to the z axis, so their periodicity is 2.16 μm in x and 0.675 μm in y. Release of Ca^{2+} from the SR can occur only at the t-tubule–SR junctions, and these sites are shown in red. The model is derived from recent experimental data in which the t-tubule–SR junctions were shown to be the sites of origin for Ca^{2+} sparks in cardiac myocytes (Shacklock et al., 1995) and from morphological data on the spatial arrangement of t-tubules in cardiac muscle (Forbes and Van Niel, 1988; Lewis-Carl et al., 1995). The SR was everywhere able to sequester Ca^{2+} (see the subsection on SR Ca^{2+} uptake, below). Ca^{2+}-binding ligands were incorporated into voxels that were not SR or t-tubule.

Calcium dynamics

As described above, the model of calcium dynamics consists of a set of simultaneous first-order differential equations describing the diffusion of Ca^{2+}, the binding of Ca^{2+} to the indicator (fluo-3) and other ligands, and the sequestration (uptake) of Ca^{2+} by the SR at each voxel within a simulated space (Fig. 3 *A*). The model is conceptually similar to those used previously for modeling the Ca^{2+} dynamics in skeletal muscle (Cannell and Allen, 1984) and cardiac muscle (Wier and Yue, 1986). The equations describing calcium dynamics are given in the following sections. (Note that, for any voxel in the simulation space (referred to by the indices i, j, and k), the rate of change in Ca^{2+} concentration is generally given as a sum of the components associated with diffusion, release, uptake, and binding of Ca^{2+} to ligands.) For brevity, Eqs. 1–4, below, address these additive components individually, without changing the notation on their left-hand sides.

Diffusion of Ca^{2+}

We modeled calcium diffusion by using a finite-difference approximation of Fick's law (Crank, 1975). For a given voxel within the cytoplasm (i.e., not SR or t-tubule and marked in black in Fig. 3 *A*), the rate of change of Ca^{2+} concentration that is due to diffusion is given by

$$\begin{aligned} d(Ca_{ijk})/dt = {} & Dx(Ca_{i+1,j,k} - 2Ca_{ijk} + Ca_{i-1,j,k})/(dx)^2 \\ & + Dy(Ca_{i,j+1,k} - 2Ca_{ijk} + Ca_{i,j-1,k})/(dy)^2 \\ & + Dz(Ca_{i,j,k+1} - 2Ca_{ijk} + Ca_{i,j,k-1})/(dz)^2, \end{aligned} \quad (1)$$

where i, j, and k are indices that point to the voxel position in the x, y, and z directions within the simulation space; dx, dy, and dz indicate the voxel dimensions in the x, y, and z directions, respectively. In FACSIMILE, the value of the diffusion coefficient for each of the three spatial dimensions (Dx, Dy, Dz) was set independently for each voxel. For "regular" voxels within the cytoplasm the three values were set equal to the experimentally measured value of the diffusion coefficient for unbound Ca^{2+} in aqueous solutions, that is, 6.0×10^{-6} cm^2/s (Hodgkin and Keynes, 1957).

The major Ca^{2+}-ligand in cardiac muscle is troponin C, which is fixed. The possibility of diffusion of Ca^{2+} that was bound to diffusible Ca^{2+}-binding ligands was not considered. In addition, fluo-3 may be largely bound, as is known to be the case for other fluorescent calcium indicators (Blatter and Wier, 1990).

In those voxels that represent the SR, the diffusion coefficients for Ca^{2+} in the direction normal to the plane of the SR were reduced by factor of 5, with appropriate modifications in Eq. 1. The SR is a network of tubules and membranous compartments with spaces between. Thus, it does not present an impenetrable barrier to Ca^{2+}. We simulated this barrier by varying the reduction factor in the diffusion coefficient value for those elements that represent the SR in the model and found a complex relation between the reduction factor and the resulting spatial spread of Ca^{2+} concentration in the model, given the presence of other processes (i.e., binding and sequestration). As a result of this sensitivity analysis we reduced the diffusion coefficient of the SR elements for Ca^{2+} to 20% of its value for regular cytoplasmic voxels as a simple way to model an otherwise complex geometrical arrangement of compartments.

SR Ca^{2+} Release

The release of Ca^{2+} from SR was modeled as a rectangular pulse of Ca^{2+} current that entered the central voxel of the simulation space from an

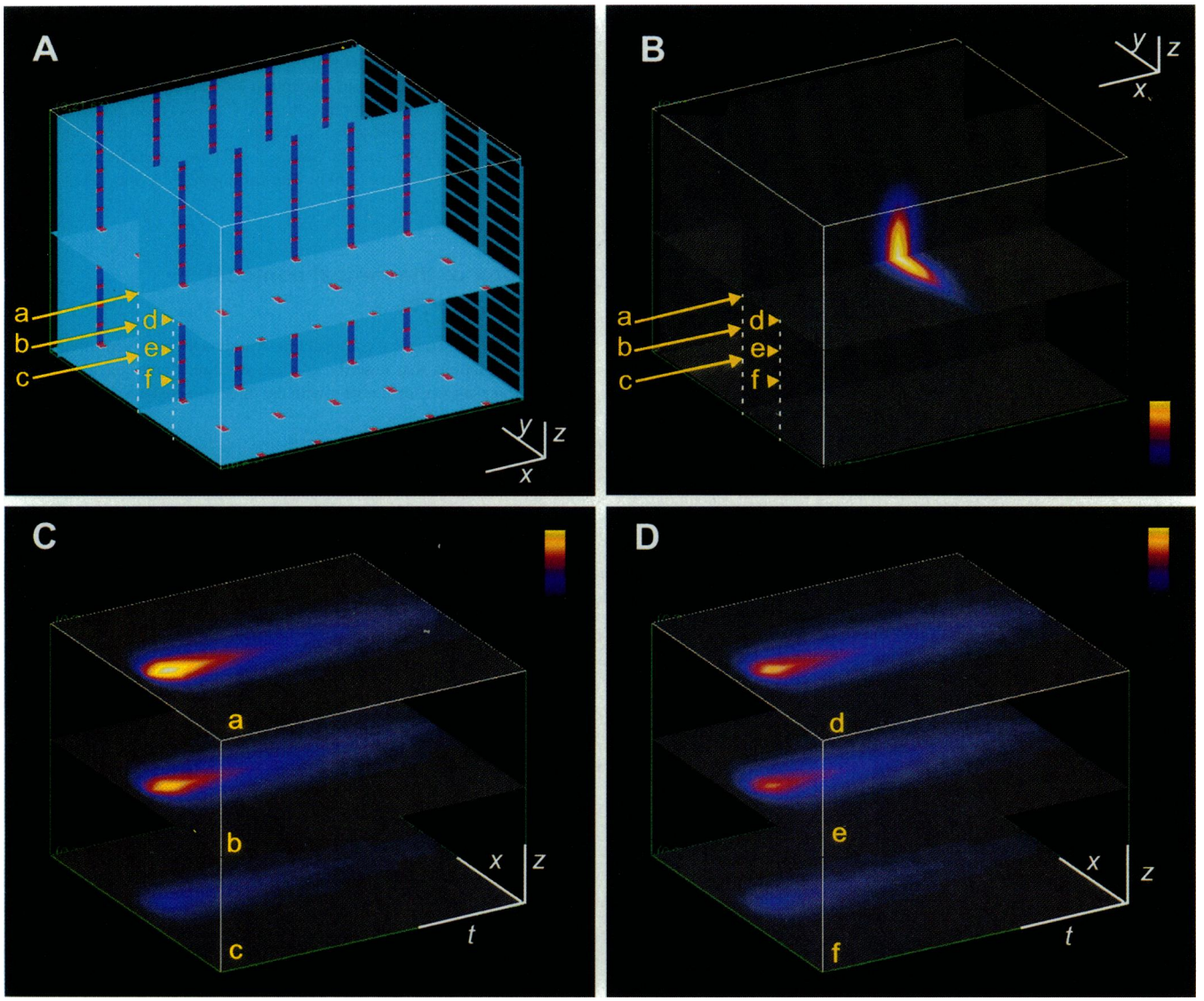

FIGURE 3 Views of a Ca^{2+} spark from different scan lines. *A*, The simulation volume represents a subcellular region of a mammalian ventricular myocyte. The entire volume had 61,952 voxels, and a voxel had the dimensions (x, y, z) of 0.271 μm × 0.135 μm × 0.135 μm for a volume of 4.94×10^{-3} μm^3. The simulation space (*central portion in A*) was 11.92 μm × 2.97 μm × 8.64 μm (x, y, z). The red elements are the sites where the release of Ca^{2+} is allowed to occur (i.e., the t-tubule–SR junctions). The magenta elements are t-tubules (i.e., no SR Ca^{2+} release or uptake), and the blue elements are SR, in which Ca^{2+} uptake occurs. The release of Ca^{2+} from the central release element produced the 3-D (confocal) image shown in *B*. In *C* and *D*, six different views (*a–f*) of this Ca^{2+} spark are shown, as would be obtained if the volume were scanned through the origin of the Ca^{2+} spark (yellow *a* in *A* and *C*), and also displaced directly downward by 1.08 μm (*b*) and 2.16 μm (*c*). Line-scan views of this Ca^{2+} spark for scans displaced laterally by 0.54 μm are shown as *d–f* (at the same depths as *a–c*). Calibration bars: in *A* and *B*, x = 2.16 μm, y = 0.68 μm, z = 1.35 μm; in *C* and *D*, t = 50 ms, x = 2 μm, z = 0.54 μm. The color scale spans the range of ratios F/F_0 from 1.0 to 3.0 (estimated $[Ca^{2+}]_i$ ~100 to ~364 nM).

adjacent voxel that was considered to be the junctional SR (i.e., next to a t-tubule). Equation 2 gives the rate of change of $[Ca^{2+}]_i$ produced by such a current:

$$d(Ca_{ijk})/dt = i_{SRR}/FZU_v, \quad (2)$$

where i_{SRR} is the SR Ca^{2+}-release channel (i.e., ryanodine receptor) current amplitude, F is Faraday's constant, Z is the valence of Ca^{2+}, and U_v is the volume of the voxel. This simplified expression for Ca^{2+} release does not take into account 1) changes in the driving force for Ca^{2+} release that may accompany changes in SR Ca^{2+} load and 2) the effects (both positive and negative) that local gradients of $[Ca^{2+}]_i$ in t-tubule–SR junctions may have on the properties of the ryanodine receptor(s). The magnitude of the SR Ca^{2+}-release current was ordinarily set at 1.4 pA, and its duration was 12 ms. These values are similar to experimental data (Rousseau and Meissner, 1989) and available estimates (Tinker et al., 1992) for cardiac SR Ca^{2+}-release channels.

Binding of Ca^{2+} to intracellular ligands

In the model, Ca^{2+} binds only to dye (fluo-3, assumed to be immobile) and to a single, immobile species of endogenous ligand (cf. Berlin et al., 1994). Binding is assumed to obey the law of mass action, with one-to-one stoichiometry. At each "regular" voxel the rate of change of $[Ca^{2+}]_i$ that

results from the binding of Ca^{2+} to dye and the endogenous ligand is given by

$$d(Ca_{ijk})/dt = k_{off,dye}[Cadye] - k_{on,dye}[Ca][dye] + k_{off,lig}[Calig] - k_{on,lig}[Ca][lig], \quad (3)$$

where $k_{on,dye}$ and $k_{on,lig}$ represent forward rate constants of Ca^{2+} binding to fluo-3 and to the endogenous ligand, respectively, and $k_{off,dye}$ and $k_{off,lig}$ represent the respective reverse rate constants. We set the values of the forward rate constants at 10^8 M^{-1} s^{-1} to ensure that the binding reactions were fast enough in comparison to diffusion and then adjusted the reverse rate constants to arrive at an apparent *Kd* that conformed to experimental data, as in Sipido and Wier (1991); see also Balke et al. (1994). The values of the parameters of Ca^{2+} binding in the model are listed in Table 1. In each of these "regular" voxels, four additional ordinary differential equations (not shown) are also integrated, giving the time courses of the free and the bound species of dye and ligand. Initial values of the four respective variables (dye, Cadye, lig, Calig) are derived from the condition of equilibrium with the resting free $[Ca^{2+}]_i$ (100 nM).

SR Ca^{2+} uptake

The rate of sequestration of Ca^{2+} by the SR is an important determinant of the rate of decline of the whole-cell or macroscopic $[Ca^{2+}]_i$-transient (Wier, 1992). In this model, spatially localized uptake of Ca^{2+} was produced by incorporation of Eq. 4 into the voxels that represent the SR. In other words, for all the voxels that contain SR, the model equations for Ca^{2+} dynamics contained a term describing the sequestration of Ca^{2+} according to the following equation:

$$d(Ca_{ijk})/dt = V_{max}(Ca_{ijk}^4/(k_m^4 + Ca_{ijk}^4) - Ca_{rest}^4/(k_m^4 + Ca_{rest}^4)). \quad (4)$$

The above dependence of the SR Ca^{2+}-uptake flux on $[Ca^{2+}]_i$ has been shown to provide the best fit for the equilibrium rates for the interaction of the SR Ca^{2+}-ATPase with Ca^{2+} in cardiac cells (Balke et al., 1994). A similar equation has been used for skeletal muscle cells (Klein et al., 1991). V_{max} was calculated as the peak amount of Ca^{2+} bound to the SR Ca^{2+}-ATPase per unit area of SR element, divided by the voxel volume, U_v. To compute the peak amount of Ca^{2+} bound to the SR Ca^{2+}-ATPase per unit area of SR element, we multiplied the SR Ca^{2+}-ATPase turnover rate, k_{max}, by the SR pump density, p_s, and by the unit area for the appropriate voxel face, U_a (see Table 1). The SR Ca^{2+}-ATPase constants were taken from Zador and co-workers (1990). The resting $[Ca^{2+}]_i$ was taken to be 100 nM.

TABLE 1 Parameters of the model

Parameter	Value
Resting calcium concentration, Ca rest	100 nM
Diffusion coefficient for free Ca^{2+}, D	6×10^{-6} cm^2/s
Voxel dimensions	
dx	0.271 μm
dy	0.135 μm
dz	0.135 μm
Voxel volume, U_v	4.94×10^{-3} μm^3
Release of calcium from SR	
Square pulse duration	12 ms
Magnitude of current, i_{SRR}	1.4 pA
Faraday's constant, F	9.649×10^4 C/mol
Uptake of calcium into SR	
Ca-ATPase turnover rate, k_{max}	0.2/ms
SR pump density, p_s	5×10^{-14} $\mu mol/\mu m^2$
unit area, U_a	3.65×10^{-2} μm^2
Michaelis constant, k_m	2.89×10^{-7} M
Binding to fluo-3	
Total dye concentration	50 μM
$k_{on,dye}$	108 M^{-1} s^{-1}
$k_{off,dye}$	50 s^{-1}
Binding to the intracellular ligands	
Total ligand concentration	134 μM
$k_{on,lig}$	108 M^{-1} s^{-1}
$k_{off,lig}$	63 s^{-1}

Formation of theoretical confocal line-scan images

Formation of the theoretical confocal line-scan images involved solving the system of equations that describe calcium dynamics and convolving the resulting three-dimensional object with the three-dimensional PSF for each moment in time.

Computation of the object

First, the system of model equations was solved by use of the FACSIMILE programming language (see Overview of the Model). FACSIMILE imposed mass conservation control (i.e., no net change in Ca^{2+} or other variables) and no-net-flux boundary conditions and utilized Gear's (1971) algorithm for ODE integration in time (solution). To produce the total solution with the available computing resources it was necessary first to obtain a smaller part of the solution in only one eighth (octant) of the simulation space ($x \geq 0$, $y \geq 0$, $z \geq 0$). We achieved this by incorporating SR Ca^{2+} release into the voxel at the lower left front corner of a simulation space that was one eighth of the total. This octant was then reflected in the appropriate directions (x, y, and z) to produce a solution with eightfold (central) symmetry. It was assumed also that fluorescence (F) was directly proportional to [Cadye] (Holmes et al., 1995). The four-dimensional function $F(x, y, z, t)$ thus obtained became the object, as if it were an actual physical specimen in which fluorescence changed with time.

FACSIMILE adjusted the time steps for optimal integration. Solutions for all the variables were sampled, however, at 2-ms intervals, as in experimental line-scan images obtained by our Bio-Rad MRC 600 confocal microscope. Typically, integration was allowed to proceed for 70 ms.

Convolution of the object with the PSF to produce the image

The image was calculated as the discrete approximation of the 3-D convolution integral of the object, F, and the PSF (Hiraoka et al., 1990):

$$Im(x, y, z, t)|_{t=ti} = Cadye(x, y, z, t)|_{t=ti} * psf(x, y, z). \quad (5)$$

Convolution was accomplished by the multiplication of the 3-D Fourier transforms of F and the PSF, by use of procedures available in the IDL software. (This required that F and the PSF have the same overall dimensions and that their voxels be the same size.) The resulting image of the idealized model Ca^2 spark at the moment that $[Ca^{2+}]_i$ peaked is shown in Fig. 3 *B*. The full widths at half-maximum level for the image intensity distribution at peak time are 0.74, 1.14, and 2.84 μm in the x, y, and z directions, respectively.

We required three steps to obtain a line-scan image given the four-dimensional function, $F(x, y, z, t)$ (image intensity distribution among the voxels of the simulated space for all the sampled moments of time): 1) sampling of certain fixed y and z coordinates to arrive at a two-dimensional array of intensity distributions along the x and t dimensions, 2) simulation of 8-bit analog-to-digital conversion by linear scaling of the intensities between 0 and a maximal value, which was set above the maximal $Im(x, y, z, t)$ (this procedure simulated level adjustment during the analog-to-digital conversion and brought the simulated images quantitatively close to the images obtained experimentally), and 3) computation of

pseudo-ratios to mimic the determination of $[Ca^{2+}]_i$ from fluo-3 images (Lipp and Niggli, 1994) by dividing all the image intensity levels by values at the region of resting $[Ca^{2+}]_i$.

Simulation of noise and 8-bit quantization

To reproduce the possible dynamic range of ratio amplitudes observed in line-scan imaging of isolated Ca^{2+} sparks we incorporated the noise that is evident in all the experimental images into the model. Because the main source of noise in such images is the shot noise of the photomultiplier tube (Sheppard et al., 1995), we simulated the noisy signal in a simplified way (cf. Holmes et al., 1995) while retaining the important property that the level of the noise increases with increases in the level of the signal. A normally distributed random variable was added at each spatiotemporal point to the Cadye variable so that, for a given point, the addition did not change the mean of the signal and the standard variation was proportional to the mean. The proportionality coefficient (usually 0.5) was varied until the appearance of the resulting ratio images had been adjusted to resemble a typical experimental record.

RESULTS

Ca^{2+} spark viewed from different scan lines

The theoretical Ca^{2+} spark (shown with cross-sections through its peak in time and space in Fig. 3 *B*) was used to simulate line-scan images as they might be obtained from various positions of the scan line with respect to the origin of the Ca^{2+} spark. This simulates viewing the Ca^{2+} spark in different ways, as happens experimentally. In Figs. 3 *C* and *D* six different views of the same Ca^{2+} spark are shown, with the scan-line positions marked as follows: the in-focus view (*a*), defocused by 1.08 μm (*b*), defocused by 2.16 μm (*c*), and then displaced by 0.54 μm from those positions (*d–f*). It is apparent from these images that the peak amplitude (i.e., the increment in the fluorescence ratio from the baseline level divided by the ratio at resting $[Ca^{2+}]_i$, where it is theoretically unity), the spatial spread (as measured at 0.1 of maximal height for the brightest Ca^{2+} spark in the population), and the rise and fall times ($T_{1/2}$) of the Ca^{2+} spark are all highly dependent on the position from which the spark is viewed. The data are summarized in Table 2.

At the central position of the scan line, labeled *a* in Table 2 and in Fig. 3, we have simulated an in-focus line scan through the origin of a Ca^{2+} spark. In Fig. 4 this simulated in-focus line scan is compared with a typical sharpest (therefore judged likely to be approximately in focus) experimental line-scan record of an actual Ca^{2+} spark. Although we did not vary the parameters of the model to fit the simulated Ca^{2+} spark to the experimentally observed data, Fig. 4 shows excellent agreement between the modeled and the experimental Ca^{2+} sparks in terms of time course at the central x position. The spatial spread of the simulated Ca^{2+} spark shown in Table 2 is approximately half that of a typical experimental Ca^{2+} spark. Thus, for our purposes the model provides a reasonably realistic presentation of the four-dimensional image profile of a Ca^{2+} spark.

Generally, with displacement in the y or the z direction of the position of the scan line relative to the origin of the Ca^{2+} spark, the peak amplitude of the image of the simulated Ca^{2+} spark decreased following an asymmetric bell-shaped curve (not shown). Changes in rise time were relatively small. Fall time increased with displacement from the origin of the Ca^{2+} spark along either the y or the z direction. However, these two functions still represent a small subset of all possible views of a Ca^{2+} spark. In general, it will be necessary to measure populations of Ca^{2+} sparks obtained from actual experimental records. Also, it is usually the case that the probability of the occurrence of Ca^{2+} sparks is reduced to a low level so that Ca^{2+} sparks can be observed in isolation from one another (López-López et al., 1994, 1995; Cannell et al., 1994). For example, if an experimental intervention is predicted to change the duration of the opening of the SR Ca^{2+}-release channel, then the finding that rise times have increased would be required to support the hypothesis. (Importantly, it would not be possible to observe the change in rise time of a single Ca^{2+} spark.) Therefore, the actual experimental data that will usually be obtained will be histograms of Ca^{2+}-spark properties, as have been published already for Ca^{2+} sparks in skeletal muscle (Tsugorka et al., 1995; Klein et al., 1996) and cardiac muscle (López-López et al., 1995; Cheng et.al., 1996). Accordingly, we have generated such population histograms, as described in the next section.

Simulation of noise

The simulation of noise, and its effects on line plots of the type usually used to derive the image parameters of Ca^{2+} sparks, are illustrated in Fig. 5. Fig. 5 *A* shows changes in the time course of the central section of the dye-bound Ca^{2+} concentration overplotted with the time course of the no-noise dye-bound Ca^{2+} concentration (Cadye) at the central point of the simulation space. Fig. 5 *B* shows the time course of the ratio image intensity at the central point of the simulation space, with and without noise. Note how these

TABLE 2 Effect of position of the scan line with respect to the origin of the Ca^{2+} spark

	Position (from Fig. 3)					
Parameter	a	b	c	d	e	f
Peak Height	1.67	1.13	0.26	1.14	0.86	0.20
Rise time (ms)	8.5	9.1	8.7	8.8	9.2	8.8
Fall time (ms)	21.7	23.0	28.0	26.6	26.4	31.5
Spread (μm)	1.58	1.48	0.64	1.53	1.40	0.36

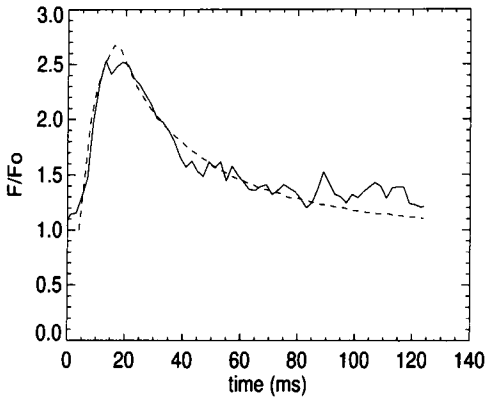

FIGURE 4 Comparison of the time courses of changes in fluo-3 fluorescence in line scans from a theoretical Ca^{2+} spark (*dashed curve*) and from a typical experimental in-focus Ca^{2+} spark (*solid curve*). Ratio images are compared at the central x position. The ordinate shows the pseudoratios of fluo-3 fluorescence. (The experimental Ca^{2+} spark was evoked from a guinea pig cardiac ventricular cell during a 200-ms voltage-clamp depolarization to +10 mV from a holding potential of −40 mV in the presence of 10 μM of verapamil to reduce the probability of an L-type Ca^{2+} channel opening.) The ratios derived from experimental data were filtered first by smoothing the image with a boxcar average algorithm with a width of 3 pixels (original pixel size 0.271 μm by 2 ms).

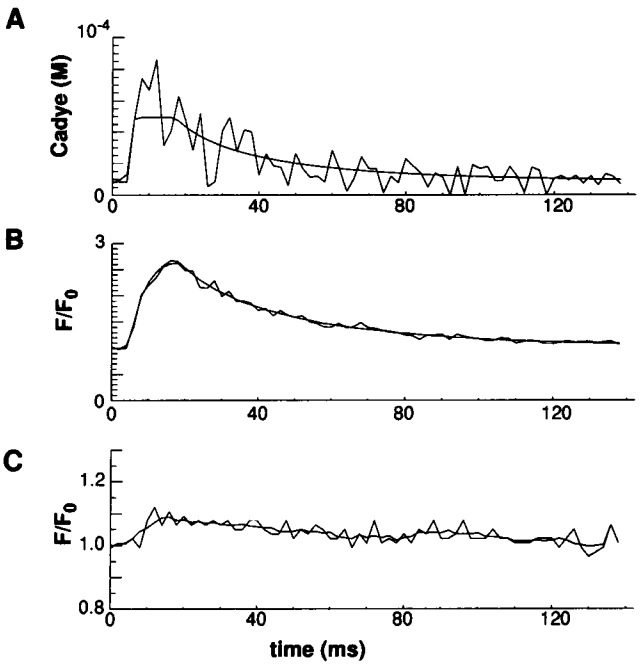

FIGURE 5 Simulation of noise. The abscissa (time) is in milliseconds. *A*, The time course of the variable (Cadye) is shown before and after the noise component is added, at the central x position. *B*, Respective time courses of the intensity of the ratio image. *C*, Time course of the intensity of the ratio image at an off-center line-scan position (dy = 0.54 μm, dz = 2.295 μm) after incorporation of noise. Overplotted is the same signal smoothed by the boxcar average technique (width, 5 pixels).

curves are smoothed compared with the curves in Fig. 5 *A*. Fig. 5 *C* shows an example of the time course of the ratio image intensity for a sample line scan that is both out of focus and laterally displaced to the origin of the Ca^{2+} spark (displacement in y and z are 0.54 and 2.295 μm, respectively). A comparison of Figs. 5 *B* and *C* illustrates the problems associated with defining the peak amplitude, rise time, and fall time for real images even for relatively small displacements of the scan line relative to the origin of the Ca^{2+} spark and a relatively high threshold (the amplitude of this ratio time course might be approximately 6–7% of the in-focus, no-noise simulated value of 1.67). To achieve a more reliable determination of the line-scan image parameters and a closer simulation of the data-processing algorithms involved in imaging Ca^{2+} sparks we subjected the simulated noisy ratio image to the same smoothing algorithms routinely used to interpret Ca^{2+} images obtained with fluo-3. A median filter, of width 3 by 3, was used to filter the rough images. This smoothing decreased only slightly the Ca^{2+} spark amplitudes (<3–5%, considered acceptable). However, the time parameters of Ca^{2+} sparks were defined much more reliably inasmuch as the filtering eliminated the inclusion of the peaks that were produced by the noise (e.g., photon noise) of the system. Therefore, in the presence of noise, smoothing was necessary, and the width of the smoothing function was chosen to eliminate high-frequency noise and to minimize confounding the determination of the time parameters of Ca^{2+} sparks.

Distribution of image properties of Ca^{2+} sparks

We simulated two experimental situations that are applicable to the observation of Ca^{2+} sparks in muscle in which SR Ca^{2+} release occurs at the junctions of the SR and the t-tubules (i.e., mammalian cardiac ventricular muscle and skeletal muscle). In both cases we assumed that the scan lines were always oriented parallel to the long (x) axis of the cell and that the experimental conditions permitted registration of isolated Ca^{2+} sparks. Both cases were analyzed with and without noise. As shown below, the presence of realistic levels of noise had substantial effects on the population histograms.

The first case (Case 1) was that of the observation of many Ca^{2+} sparks with scan lines selected randomly. Under these conditions the distribution of the apparent Ca^{2+}-spark parameters will arise from taking into account all possible positions of the scan line relative to the origin of a Ca^{2+} spark. This simulates the usual experimental situation, in which it is not possible to select a scan line that will pass through the site of origin of a Ca^{2+} spark. The simulation procedure involved viewing the spark of Fig. 3 *A* and *B* from every possible line-scan location in y and z and determining the rise time, the fall time, and the peak height. A small threshold (3% relative to the peak amplitude level) was set for the ratio values. The calculated frequency histogram for the peak amplitude of the line-scan image is shown in Fig. 6 *B*. To facilitate an understanding of how the histogram shape is related to the intensity profile of the simulated image from Fig. 3 we plotted the time courses of line-scan ratio images of the theoretical Ca^{2+} spark viewed

from locations *a–f* (see Fig. 3) in Fig. 6 *A* and then marked the appropriate distribution bins where these locations give their input. In this case, however, there are also many intermediate inputs from all the other displacement values within the simulation space, so all the bins accrued nonzero values and the number of occurrences changed more or less monotonically with the value of the peak amplitude. Fig. 6 shows that the amplitude distribution is skewed toward lower values compared with the properties of the in-focus Ca^{2+} spark and that the distribution is not Gaussian (normal).

The second case (Case 2) that was analyzed was that of the microscope objective focused onto the site of origin of a Ca^{2+} spark, as is possible in mammalian ventricular muscle in which t-tubules can be localized (Shacklock et al., 1995), and when many images were acquired from the repeated scanning of one line. The resulting distributions of the image properties would be the same as in Case 1 (above) if Ca^{2+} sparks could originate, with equal probability, from any given point in the specimen. However, only certain points (i.e., the t-tubule–SR junctions) in the specimen can be the sites of SR Ca^{2+} release (see Fig. 3 *A*). The calculated amplitude histogram (Fig. 7 *B*) indicates that this distribution is skewed toward lower values, and it is not Gaussian (normal) or unimodal. In contrast to Case 1, this distribution has distinct peaks that reflect the fact that the Ca^{2+} sparks have arisen from only certain locations in the cell volume. To illustrate this issue, in Fig. 7 *A* we have plotted the time courses of the ratio image intensity for the line-scan location at the origin of the Ca^{2+} spark and with displacement of one sarcomere in each direction. Therefore, these plots represent input from the nearest-neighbor sites of possible origins of Ca^{2+} sparks. Unlike for Case 1, no intermediate values are possible for the range between the values of group *a–c* and the values of group *d*, *e* (see Fig. 7 *B*). The histogram falls into more than one cluster owing to the discrete nature of possible SR Ca^{2+}-release sites, which results in certain gaps in possible signal heights registered at a given observation point.

For both Cases 1 and 2 similar histograms were generated for rise and fall times (T_{rise} and T_{fall}; see the previous section). These histograms are not shown, as their shape was found to be especially sensitive to the value of the threshold.

Effects of noise

The analysis of the ratio images of the noisy simulated data required a threshold of 7–10% (so only Ca^{2+} sparks with amplitudes varying by a maximum of 10–15 times could be quantified from a population of images) to identify reliably the parameters of Ca^{2+} sparks. The peak amplitude distributions generated with the simulated noisy signal and a threshold set at a level of 0.1 are presented in Fig. 6 *C* for the case of the random placement of the scan line (Case 1) and in Fig. 7 *C* for the case of the repeated scanning of a fixed line (Case 2). Noise does not change the general shape of the amplitude distributions for the two experimental cases. In both cases the amplitude histograms remain skewed to smaller values (asymmetric, non-Gaussian), and

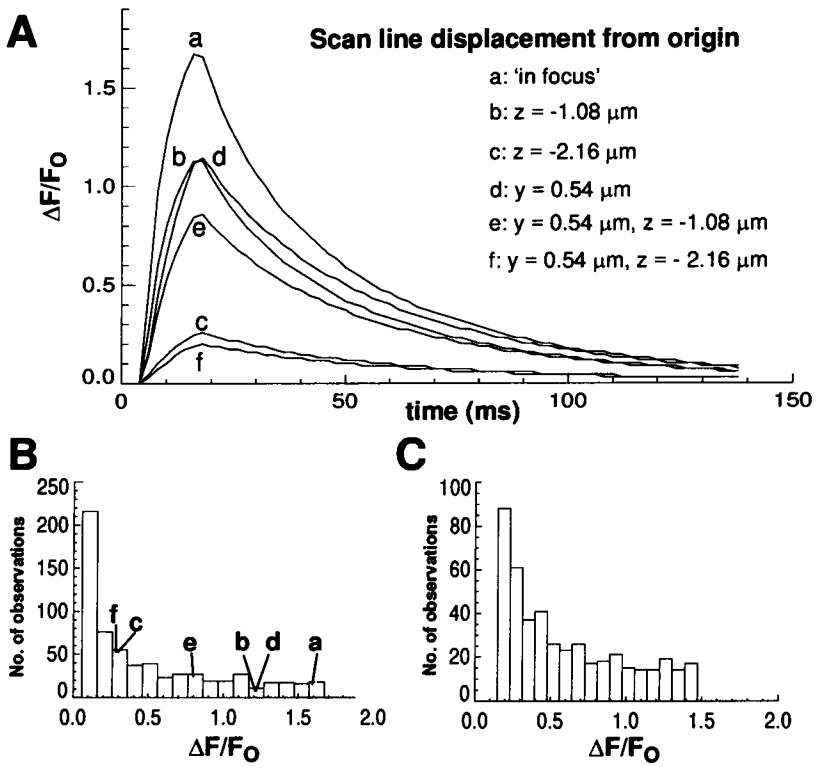

FIGURE 6 Case 1: Ca^{2+} spark viewed from different scan lines (i.e., at different displacements from the site of origin). *A*, Line plots of the Ca^{2+} spark; *a–f* correspond to the positions of the scan line as shown in Fig. 3 and noted above as displacements. *B*, Frequency distribution histograms of all possible Ca^{2+}-spark amplitudes shown without noise. The threshold level is 3%. *C*, Frequency distribution histograms of all possible Ca^{2+}-spark amplitudes (same as *B*) shown with noise. The threshold level is 10%. When the scan line is selected randomly in relation to the origin of a Ca^{2+} spark, the histogram of observed amplitudes is skewed to the lower values.

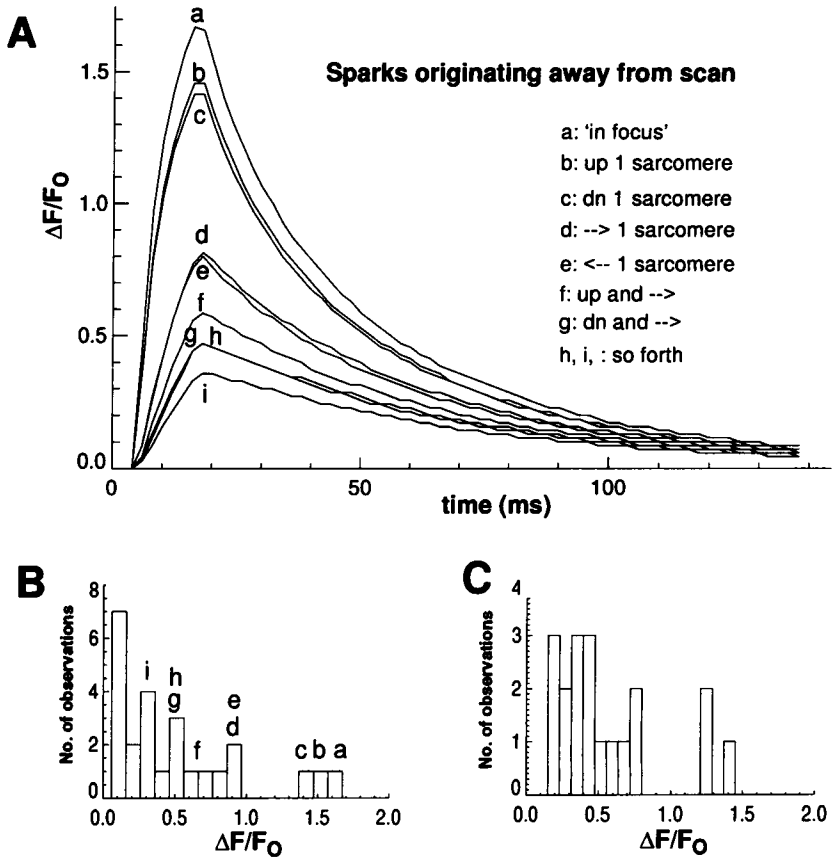

FIGURE 7 Case 2: Ca^{2+} sparks viewed from a fixed position. *A*, Line plots of Ca^{2+} sparks; *a–i* correspond to Ca^{2+} sparks arising at the site of the scan line site and at a distance of one sarcomere above, below, and to the sides of the sarcomere through which the scanning is ocurring. *B*, Frequency distribution histograms of all possible Ca^{2+}-spark amplitudes without noise. The threshold level is 3%. *C*, Frequency distribution histograms of all possible Ca^{2+} spark amplitudes with noise. The threshold level is 10%. When the position of the scan line is fixed, the histogram of observed amplitudes has peaks because Ca^{2+} sparks can arise only at a certain other places (i.e., t-tubule–SR junctions) that have a fixed geometric relation to the region being observed.

for Case 2 they show distinct peaks. However, in the presence of noise (and the associated filtering procedures) the distributions appear smoother. Increasing the threshold makes the histograms sparser and removes the influences from remote points, so the histogram assumes a more complex shape even in Case 1 and falls into several distinct components in Case 2. Fig. 8 presents histograms for the rise time (Fig. 8 *A*) and the fall time (Fig. 8 *B*) for Case 1. (For Case 2 the number of voxels with a Ca^{2+} signal large enough to permit us to calculate reliably T_{rise} and T_{fall} was too small to generate statistically informative histograms.) The distribution of rise times is rather narrow and indicates that it is determined largely by the contribution of out-of-focus fluorescence. The distribution of fall times is skewed to longer times and reflects the fact that Ca^{2+} diffuses slowly into the region being observed, producing additional fluorescence to that being detected from other regions.

Effects of diffusion and blurring on the simulated line-scan images of the Ca^{2+} spark

The rigorous study of the combined influences of Ca^{2+} diffusion and binding and of blurring by the confocal optical system required the development of the comprehensive simulation system described in this study. We also attempted to evaluate the relative importance of the above factors in a more simplified way. We estimated the relative contributions of these two components to the total simulated signal, that is, the original, no-blurred part of the signal, and the remaining blurred part of the signal. Fig. 9 shows the effects of each component on line plots taken through the central x position in a line-scan image of a simulated Ca^{2+} spark at various displacements of the scan line relative to the origin of the Ca^{2+} spark. Both the no-blurred (*dashed curves*) and the blurred (*solid curves*) signal intensities were normalized to their respective maximal values. Both components of the signal decayed rapidly in space with displacement of the scan line from the origin of the Ca^{2+} spark. It is clear that, with the given model parameters and the measured PSF, 1) both Ca^{2+} diffusion–binding and blurring make substantial contributions to the resulting spatial profile of the fluorescence signal, 2) there is an asymmetry in the image formation, so blurring is much more important with axial than with lateral displacements, and 3) simultaneous displacement of one sarcomere in both the y and the z directions (Fig. 9 *D*) attenuates the blurred signal by approximately half of its peak level and the no-blurred signal by more than 85% of its maximal value. This asymmetry in the rate of spatial decay is not due entirely to the asymmetries of the PSF because the no-blurred portion of the signal is attenuated more with a one sarcomere displacement in the y direction than with a one sarcomere displacement in the z direction. Hence the quantitative relations of

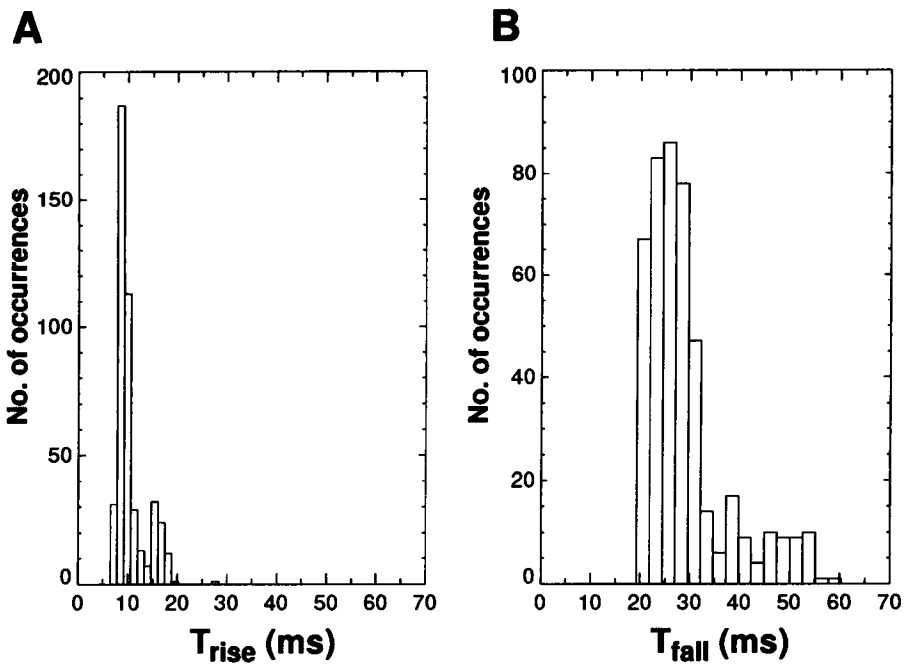

FIGURE 8 Rise times and fall times of a Ca^{2+} spark for Case 1 (Ca^{2+} sparks viewed from all possible positions). The distribution histograms for the rise times (*A*) and the fall times (*B*) of a simulated Ca^{2+} spark are shown. A random position of the scan line is assumed, and noise is incorporated. The threshold level is 10%. The abscissa (parameter value) is in milliseconds. The ordinate represents the number of occurrences.

the spatial asymmetry are different for the resulting image and for the PSF profile.

We also evaluated the possibility that the displacement-dependent changes in the amplitude histograms for Cases 1 and 2 presented above were a consequence of the departure of the experimentally determined PSF from the theoretical PSF. Inasmuch as the measured axial spread of the PSF for our confocal system was roughly twice the theoretical limit for confocal microscopes (due, in part, to the pinhole aperture's being adjusted typically to a partially open position as a trade-off between optical sectioning and signal acquisition), we repeated the whole set of procedures for the simulation of line-scan images and for the generation of amplitude histograms, using a corrected PSF obtained by shrinking the experimentally determined PSF twofold in the z dimension. As shown in Fig. 10 for both Cases 1 and 2, the normalized amplitude histograms obtained by use of the corrected PSF (*solid lines*) are not significantly different from the normalized amplitude histograms obtained with the experimentally determined PSF. In absolute terms, the peak ratio amplitudes are higher at the central portion of simulated space and the rate of spatial decay rate is steeper when the PSF is axially shrunk.

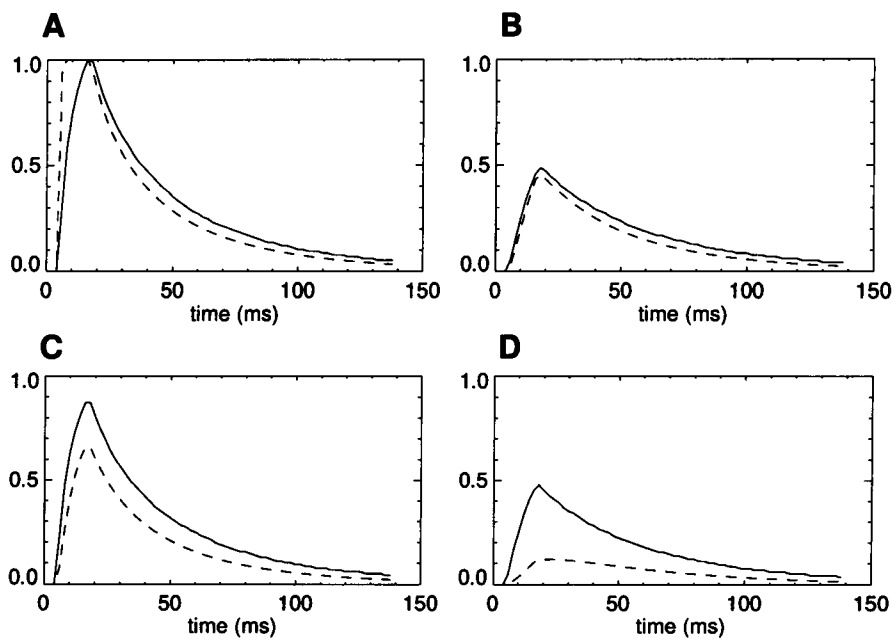

FIGURE 9 Effects of diffusion and blurring on the time course of a Ca^{2+} spark at central x position in the line-scan image. The solid curves denote the normalized pseudoratio (i.e., blurred signal), and the dashed lines represent the normalized Cadye value (no-blurred signal). The abscissa represents time (milliseconds), and the ordinate shows normalized pseudoratio (*solid curves*; blurred signal) and the normalized Cadye signal (*dashed curves*; no-blurred signal). *A–D*, Various displacements of the scan line from the site of origin of the Ca^{2+} spark: *A* represents the case in which the scan line passes through the site of origin of a Ca^{2+} spark (i.e., in-focus z position with no lateral displacement). *B* shows the effect of displacing the scan line by one sarcomere in the y direction (laterally). *C* illustrates the case in which the scan line is displaced one sarcomere in the z direction (axially). *D* shows the consequences of displacing the scan line by one sarcomere in both the y and the z directions.

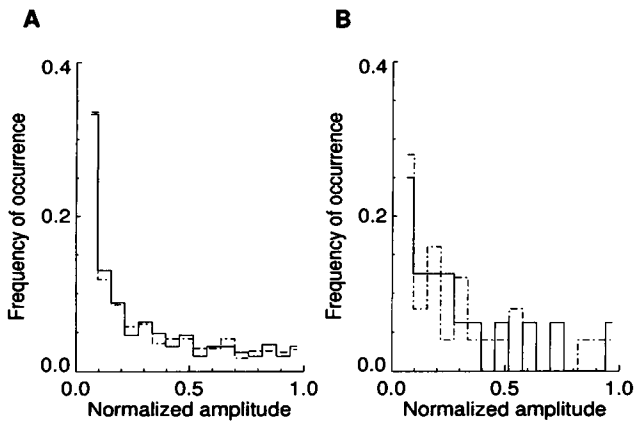

FIGURE 10 Effects of changes in the axial width of the PSF on the frequency distributions of peak amplitudes of the Ca^{2+} sparks in Cases 1 (*A*) and 2 (*B*). The solid lines denote the envelopes of the amplitude histograms as simulated with the PSF shrunk twice in the z direction (axially) compared with the experimentally determined 3-D PSF of our confocal microscope. The dashed–dotted lines outline the envelopes of the amplitude histograms simulated with the experimentally determined PSF (see Fig. 2).

Practical considerations for measured amplitude distributions

In practice, the peak amplitude histograms of the simulated Ca^{2+} spark shown in Figs. 6 and 7 (both with and without noise) cannot be compared directly with the peak amplitude histograms obtained from experimentally determined Ca^{2+} sparks. This is so, in part, because of the inability of the model to account for all the subjective factors that are involved in the selection and processing of actual line-scan images of Ca^{2+} sparks. For example, the model does not consider the variability in an observer's ability to discriminate visually an elevation in $[Ca^{2+}]_i$ on a noisy background as a Ca^{2+} spark (Pawley, 1995). In addition, in spite of adjustments for noise and threshold, the model is still unable to identify with equal probability both Ca^{2+} sparks with amplitudes that fall into the leftmost bins and Ca^{2+} sparks whose amplitudes are close to maximal. There are several reasons to introduce a transfer factor to take into account the statistical reliability of identifying a Ca^{2+} spark as a function of its amplitude relative to the maximum value (i.e., defining the color code chosen in image processing). Even in the absence of noise, the reliability of Ca^{2+}-spark detection varies monotonically with its brightness with respect to background, in a manner similar to that in the Weber experiments on brightness discrimination (see a discussion in Russ, 1995). The complications of noise can be resolved, to some extent, by incorporation of the Rose criterion (Pawley, 1995) for pixel discrimination (i.e., reliable discrimination is assumed to require a fivefold excess of pixel brightness over the baseline level of noise) in the processing of the signal. However, in our application the problem of object discrimination against the noisy background is complicated further because ratio images are being analyzed and often only incremental variations in ratios are informative. During this type of processing the noise component of the signal is subject to complex nonlinear transformations. As a practical solution to this problem we used an empirically derived visibility factor to translate the amplitude histograms for simulated Ca^{2+} sparks into amplitude histograms for experimentally measured Ca^{2+} sparks. Fig. 11 *A* shows the visibility factor, which is a sigmoid function constructed to represent the reliability of detecting a Ca^{2+} spark against a background with the typical noise characteristics of ratio images. The function represents the fraction of Ca^{2+} sparks at a given amplitude that would be detected in a large population of noisy images. Therefore, it approaches unity for higher relative amplitudes and stays close to zero for relative amplitudes below 10–20% of the maximal amplitude. Although this function is an assumed, simplified relation, it was chosen after we analyzed the noise levels (and variations thereof) in experimental line scans and was produced by convolution of a piecewise-linear function (chang

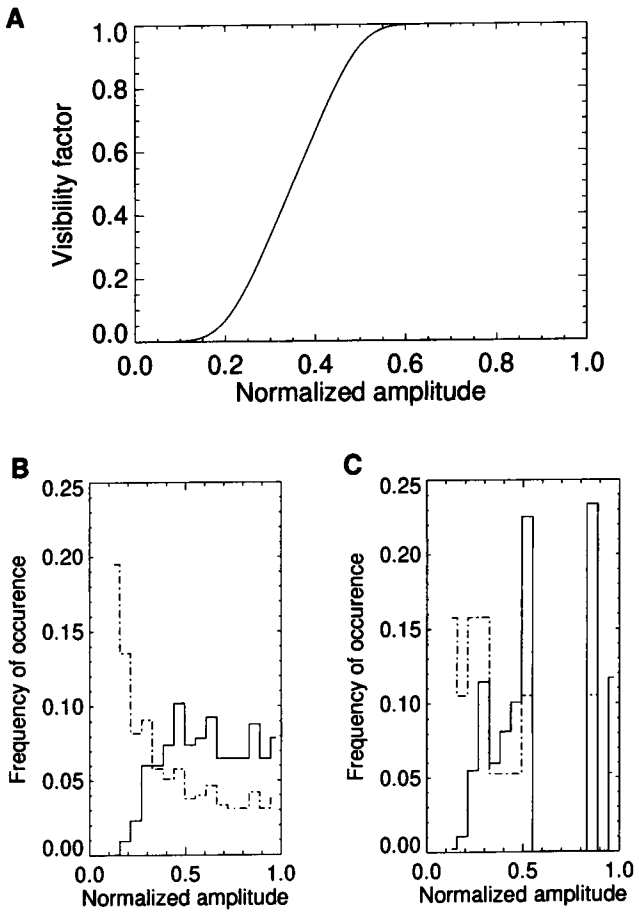

FIGURE 11 Practical implications for the histograms of Ca^{2+}-spark amplitudes in both Cases 1 and 2 for noisy data. *A*, Assumed visibility factor as a function of normalized height of the Ca^{2+} spark. *B*, *C*, Theoretical distribution of the amplitudes of Ca^{2+} sparks with noise incorporated into the simulations (*dashed–dotted lines*) and the predicted experimentally derived distribution of the amplitudes of Ca^{2+} sparks adjusted for visibility (*solid lines*) for Case 1 (*B*, Ca^{2+} sparks viewed from a random scan-line position) and for Case 2 (*C*, scan line going through a SR Ca^{2+}-release site).

ing from 0 to 1 at an abscissa interval from 0.2 to 0.5) with a Gaussian kernel of width 0.05. This technique allowed us to incorporate subjective factors involved in the evaluation of Ca^{2+} sparks from experimental line-scan data and to provide a reasonable estimate of the shape of the predicted amplitude histogram according to our model. The resulting peak amplitude histograms are depicted in Fig. 11 *A* (Case 1: Ca^{2+} sparks viewed from all possible positions) and *B* (Case 2: scan line position fixed). In Case 1 the resulting distribution is close to monotonic and unimodal, and its peak underestimates the in-focus amplitude. In Case 2 the distribution of peak amplitudes is separated into more than one component. In both cases the distributions are neither symmetric nor Gaussian.

SUMMARY AND DISCUSSION

Interpretation of the line-scan confocal images of $[Ca^{2+}]_i$

Currently, the prevailing theory in cardiac excitation–contraction coupling is the local control theory, in which spatially localized $[Ca^{2+}]_i$ transients, or Ca^{2+} sparks, arise when Ca^{2+} enters the cytoplasm through a single L-type Ca^{2+} channel and establishes a local increase in $[Ca^{2+}]_i$ that activates closely associated SR Ca^{2+}-release channels (ryanodine receptors) (Stern, 1992; Cannell et al., 1994, 1995; López-López et al., 1994, 1995; Niggli and Lipp, 1995; Shacklock et al., 1995). Ca^{2+} sparks play an important role in excitation–contraction coupling at the level of the sarcomere, and macroscopic (whole-cell) $[Ca^{2+}]_i$ transients are understood in terms of the spatial and temporal summation of many such events (Stern, 1992; Niggli and Lipp, 1995; Cannell et al., 1995; López-López et al., 1995; Tsugorka et al., 1995). Although Ca^{2+} sparks have been observed with laser scanning confocal microscopy and the Ca^{2+}-sensitive fluorescent indicator fluo-3, the quantitative evaluation of their kinetic characteristics has been difficult. Because line-scan confocal images contain only one spatial dimension, important spatiotemporal information is missing from typical experimental records. In the present research we developed a comprehensive model to overcome these difficulties. In simplified form, it represents all the stages of data processing inherent in imaging Ca^{2+} sparks with fluo-3, from the initial SR Ca^{2+}-release event to the resultant line-scan confocal image, as it would be measured under real experimental conditions. Blumenfeld and co-workers (1992) implemented an analogous approach to the problem of the interpretation of microscopic fura-2 records of $[Ca^{2+}]_i$ transients in *Aplysia* neurons. By considering the important factors of Ca^{2+} dynamics and of the processes involved in the formation of the image the model was able to determine the properties of the line-scan confocal images of an idealized Ca^{2+} spark. By combining the simulation of the step-by-step measurement process with the specific optical characteristics of the confocal microscope the model explored how the idealized Ca^{2+} spark is altered during the measurement process that finally yields the line-scan image. As a result, it was apparent that the image of a Ca^{2+} spark depends on the way in which the Ca^{2+} spark was viewed (Figs. 3 *C* and *D*, 6 *C* and *D*, 7 *C*and *D*, 8, and 11). The model simulations provide a quantitative assessment of the effect of the imaging process on the analysis of Ca^{2+} sparks and show how this imaging process can affect the properties histograms of stereotyped Ca^{2+} sparks.

Model of Ca^{2+} dynamics

A number of theoretical models have focused on various aspects of the dynamics of Ca^{2+} in cardiac cells (see the review by Stern (1992) and Wier and Yue, 1986; Backx et al., 1989; Blatter and Wier, 1990; Pratusevich et al., 1987; Bett, 1995). The model presented here differs from previous ones (Backx et al., 1989; Blatter and Wier, 1990; Wier, 1992) in the way in which the definition of the complex geometry of intrasarcomere space incorporates sites for the uptake and release of Ca^{2+} and specifies the spatial pattern for the binding processes. The model takes into account all the major processes that shape Ca^{2+} sparks. The relatively close fit to typical experimental records (Fig. 4) testifies to the reasonableness of the set of assumptions that were used in the model. The spatial organization of the idealized orthogonal grid (Fig. 3 *A*) was chosen as the simplest way to combine all the processes of Ca^{2+} dynamics in a single finite-difference scheme, although it is likely that refinement of the topological aspects of the model, as well as the incorporation of a term for the diffusion of mobile dye, will further improve the quantitative fit to the spatial characteristics of a reference Ca^{2+} spark.

Calcium buffering can be incorporated into the model by one of two possible methods: 1) by use of the value of the apparent diffusion coefficient reported in the literature (Bers and Peskoff, 1991; Wagner and Keizer, 1994), or 2) by use of the value of the diffusion coefficient for free Ca^{2+} in aqueaous solutions (Blatter and Wier, 1990; Blumenfeld et al., 1992) and explicitly incorporating chemical interactions with buffers into the model equations. We took the latter approach for two reasons. To determine the emitted fluorescence we were interested in predicting correctly the distribution of one of the Ca^{2+} buffers, fluo-3. In addition, there is evidence (Wagner and Keizer, 1994) that the components both of diffusion and of the nonequilibrium chemical reactions in the combined model equations cannot be neglected under most of experimental conditions encountered in fluorescent dye imaging of $[Ca^{2+}]_i$.

We modeled the SR Ca^{2+} pump by using parameters taken from literature (Balke et al., 1994; Zador et al., 1990), but an exact comparison of the parameter values is not straightforward. Instead of modeling the SR space by matching its fractional volume and surface geometry, we simplified the simulation of Ca^{2+} uptake by adding appropriate Ca^{2+} sink terms to the elements representing the location of the SR. The resulting rate of Ca^{2+} efflux in these locations allowed the time course of the simulated Ca^{2+}

spark to fit a typical experimentally determined Ca^{2+} spark (Fig. 4). Hence, the combination of the microscopic SR Ca^{2+} pump parameters with other model parameters that influence the decay of the Ca^{2+} spark was appropriate to ensure that SR Ca^{2+} uptake is fast enough to account for the decay of the $[Ca^{2+}]_i$ transient (Bers, 1991; Balke et al., 1994). However, the individual SR Ca^{2+} pump parameters from Table 1 will need further refinement when direct experimental measurements become available. The SR Ca^{2+} pump density was set at a theoretical maximum for a protein of that size (Zador et al., 1990), in agreement with experimental data from permeabilized myocytes (Mattiazi et al., 1994), which showed that the SR Ca^{2+} pump was close to maximal activation. Additional assumptions permitted indirect comparisons of the SR Ca^{2+} pump characteristics used here with those taken from the literature. Although we used the k_m value of 0.289 μM taken from the best fit to experimental data (Balke et al., 1994), the k_m in our model is related to the SR elements of the simulation space rather than to the accessible cell volume. In its simplified form the model did not distinguish between nonaccessible cell volume (i.e., nonmitochondrial volume) and total cellular volume. The relation of the microscopic SR Ca^{2+} pump parameters to the apparent pump constants comparable with those reported in the literature depends on the spatial organization of the model. In our model the Ca^{2+}-uptake flux per unit cell volume was 1.0597 nmol s^{-1}, but this value will decrease by a factor of 3 if the spatial discretization is made three times finer. The corresponding value of V_{max} measured in SR vesicles varied near the value of 150 μmol kg^{-1} wet wt s^{-1} (estimated to correspond to approximately 206.2 μM s^{-1}) and was too low to account for the relaxation processes in vivo (Bers, 1991). Using available estimates of the SR Ca^{2+}-ATPase in cardiac cells of 5.9 μmol kg^{-1} wet wt (Bers, 1991; which amounts to roughly 0.7 g protein/l^{-1}), the maximal flux of our simulated SR Ca^{2+} uptake was 23.8 nmol min^{-1} mg^{-1}. This approximates the estimate of 31 nmol min^{-1} mg^{-1} derived by Balke et al. (1994) at 21°C in rat cardiac cells (which corresponds to 174 nmol min^{-1} mg^{-1} at 37°C) and conforms to the measurements of Wimsatt et al. (1990) at 37°C in permeabilized rabbit ventricular myocytes (160 nmol min^{-1} mg^{-1}). Thus, the model achieves a realistic representation of the net flux of SR Ca^{2+} uptake, as shown in Fig. 4. However, this result is achieved, in part, by use of elevated values for both the SR Ca^{2+}-pump turnover rate and the SR Ca^{2+}-pump density to compensate for the model's lower SR membrane surface.

Model of the image-formation process

In our model an actual PSF was experimentally determined by use of our confocal imaging system, and the influence of the experimentally determined PSF on the resulting images was studied systematically. Although experimentally determined PSFs were reported previously for conventional epifluorescence microscopes (Agard et al., 1989; Hiraoka et al., 1990; Blumenfeld et al., 1992) and for confocal systems (Shaw, 1995), it was important to have information regarding the PSF for the specific experimental setup under conditions used during experiments with living cells (Hiraoka et al., 1990; Shaw, 1995). We used phagocytic cells to immobilize subresolution fluorescent beads to bring the refractive index of the mounting medium closer to that of the cytoplasm of a living cell. The shape of the experimentally determined PSF corresponded closely to that depicted by Shaw (1995). With our system configured for experiments with cardiac cells (i.e., partially open confocal aperture), the axial resolution as manifested by full width at half-maximum in the z direction was slightly poorer than theoretically possible with the best-aligned system. Figure 10 shows simulations that prove that the slightly less than ideal characteristics of our confocal setup did not play a substantial role in the results of this study. Specifically, these calculations show that the amplitude histograms of Ca^{2+} sparks obtained with the experimentally determined PSF are similar qualitatively to the amplitude histograms of Ca^{2+} sparks obtained with the PSF modified to reduce its axial spread to that of the theoretical limit of the confocal microscope.

The present research combines, for the first time, the analysis of line-scan image formation with the details of the quantization of signal level and the effects of noise. It also presents an empirically derived procedure to account for the subjective aspects involved in processing the images of Ca^{2+} sparks. Our simulation system permitted the evaluation of the parameters of Ca^{2+} dynamics and blurring by the confocal microscope into the resulting line-scan images and showed that the influence of both factors is substantial. However, the general properties of the amplitude histograms would not change significantly if the PSF of the confocal microscope were modified in the axial direction (shrunk twice); hence the results of the present study are setup independent. Because the characteristics of line-scan images are dramatically dependent on the position of the scan line, the quantitative parameters of the Ca^{2+} profile of an individual line-scan image cannot be determined reliably.

Practical implications of the simulation results

In the present study, for a known spatiotemporal profile of a Ca^{2+} spark the quantitative characteristics of line-scan images were predicted by the use of simulations. These characteristics were in the form of properties histograms (Fig. 11) of a line-scan image of a standard, stereotyped Ca^{2+} spark. A modeling approach that combined the simulation of Ca^{2+} dynamics with the simulation of the processes of image formation was the most useful in relating quantitatively the parameters of line-scan confocal images of Ca^{2+} sparks to the actual profile of $[Ca^{2+}]_i$. In Case 1 (Ca^{2+} sparks viewed from all possible positions) the am

plitude histograms were non-Gaussian and skewed to lower values than the amplitude histograms of in-focus Ca^{2+} sparks owing to diffusion of Ca^{2+} and blurring. In Case 2 (scan line position fixed) the amplitude histograms were neither Gaussian nor unimodal, because Ca^{2+} sparks arose only at a limited number of places in relation to an in-focus Ca^{2+}

The observation that stereotyped Ca^{2+} sparks gave rise to asymmetric distributions of image properties puts certain restrictions on the legitimacy of deconvolution procedures that rely on the assumption that identical Ca^{2+} sparks would be viewed on a line-scan image as identical images (Cannell et al., 1994). Similar uncertainities apply to the use of a 360° rotation of a Gaussian fit to a one-dimensional spatial distribution of fluorescence ratios to reconstruct the spatiotemporal properties of Ca^{2+} sparks from line-scan images (Nelson et al., 1995). As shown in the present study, the distributions of the 3-D image intensities were neither Gaussian nor rotationally symmetric because of two factors. First, the solution of the model equations for Ca^{2+} dynamics differs from the solution for diffusion from a point source because of the spatial nonuniformity of binding and uptake sites and the effect of their kinetics. Second, the experimentally determined PSF of the confocal microscope is not rotationally symmetric. Thus, the above procedure provides only an approximation of the spatiotemporal characteristics of a Ca^{2+} spark. Furthermore, the striking conclusion from the results of the present study is that the observation of identical events may result in amplitude histograms that segregate into more than one subpopulation, seemingly suggesting that the underlying Ca^{2+} profiles represent different classes of SR Ca^{2+}-release events. Therefore, whereas analysis of line-scan images of actual experiments by fitting Gaussian functions to the property histograms of Ca^{2+} sparks (Tsugorka et al., 1995; Klein et al., 1996) might be a reasonable first approximation in the evaluation of multicomponent distributions, it is not a reliable method for discriminating among different types of events.

The first stage in analyzing line-scan images of Ca^{2+} sparks was to single out individual Ca^{2+} sparks and then ascribe some quantitative values to their characteristics. With noise and the low-contrast conditions that are characteristic of most experimental situations there is a certain subjectivity in the extraction of individual Ca^{2+} sparks from the line-scan images. The present study addressed the effects of such subjectivity on the resulting properties histograms. As not all the smaller-amplitude sparks will be extracted reliably from the noisy data, the lower bins in the peak amplitude histogram (Figs. 7 and 8) will be underestimated. There will be also distortions in the time-parameter distributions, largely in the rightmost bins of the histograms. In our model the notion of threshold provided the objective criterion for incorporation of Ca^{2+} sparks of a certain size into the calculated properties distribution. Selecting a threshold high enough relative to the amplitude of the noise prevented distortions of the properties histogram by unreliable feature extraction from low-amplitude traces. Furthermore, the visibility problem was treated to incorporate into the simulation of the frequency histograms the extent of reliability of registering Ca^{2+} sparks of varying amplitude against the noisy background of typical ratio images. Thus, for the first time, the amplitude distributions obtained from the analysis of theoretical line-scan images of stereotyped Ca^{2+} sparks can be compared directly with the amplitude histograms obtained from the analysis of actual line-scan images of Ca^{2+} sparks obtained from living cells.

The simulations show the limits in the spatial localization of the origin of Ca^{2+} sparks, for example, with respect to the t-tubules (Shacklock et al., 1995). The calculated half-maximum widths of Ca^{2+}-spark image intensity distribution suggest that, whereas localization of Ca^{2+}-spark origin sites might be accurate enough in the x and the y directions, the blurring in the z direction prevents the submicrometer resolution of the site of origin of a Ca^{2+} spark. The present study shows that, in general, it is difficult to distinguish small, in-focus Ca^{2+} sparks from large, out-of-focus Ca^{2+} sparks. There is a smooth dependence of Ca^{2+}-spark appearance on the position of the scan line. The reliable classification of Ca^{2+} sparks and distinguishing subpopulations is possible only by analysis of large populations of Ca^{2+} sparks. Our results imply that each subpopulation of Ca^{2+} sparks will contribute an additive component with a shape similar to that shown in Fig. 11 to the cumulative distribution of the image properties. With future refinements, the simulation procedure can be used to check observed changes in the distribution of Ca^{2+} spark properties with the distributions predicted by the model. In this way, specific hypotheses regarding cardiac excitation–contraction coupling can be tested.

The present model has certain limitations, including 1) the absence of a factor accounting for the mobility of the Ca^{2+} indicator, fluo-3; 2) the lack of an allowance for the linear error in positioning of the focal plane with respect to the lattice of possible SR Ca^{2+}-release sites (Case 2); 3) the lack of an allowance for the component of noise associated with the scanning of the confocal microscope; and 4) an assumed ideal angular alignment of the scan line with respect to the orthogonal lattice of the SR Ca^{2+}-release sites, even though small angles between the scan line and the long axis of the cell are present in actual experiments and can be predicted to modify the shapes of resulting histograms. In addition, the geometry of SR and the free diffusion space within cardiac myocytes is probably not so simple and regular as the relationships used in the model. Using high-resolution confocal imaging of rat cardiac myocytes, Parker and Wier (1996) showed recently that SR Ca^{2+}-release sites are packed closely and irregularly in transverse planes at the Z lines. The possibility that diffusion may be restricted more transversely than longitudinally will need to be considered in further refinements of the model. Despite these limitations, the present study represents the first comprehensive attempt at modeling some of the complexities in the relationship between the properties

of Ca^{2+} sparks determined from confocal line-scan images and the actual profile of $[Ca^{2+}]_i$ within the cell.

We thank W. Gil Wier for valuable help and discussions and J. D. Hasday for providing us with the alveolar macrophages that were used in measurements of the PSF of our confocal microscope.

This research was supported, in part, by National Institutes of Health grants HL29473, HL02466, and HL50435.

REFERENCES

Agard, D. A., Y. Hiraoka, P. Shaw, and J. W. Sedat. 1989. Fluorescence microscopy in three dimensions. *Methods Cell Biol.* 30:353–377.

Backx, P. H., P. de Tombe, J. H. K. Van Deen, B. J. M. Mulder, and H. E. D. J. ter Keurs. 1989. A model of propagated calcium-induced calcium release mediated by calcium diffusion. *J. Gen. Physiol.* 93:963–977.

Balke, C. W., T. M. Egan, and W. G. Wier. 1994. Processes that remove calcium from the cytoplasm during excitation-contraction coupling in intact rat heart cells. *J. Physiol. (Lond.)* 474:447–462.

Berlin, J. R. 1995. Spatiotemporal changes of Ca^{2+} during electrically evoked contractions in atrial and ventricular cells. *Am. J. Physiol.* 38:H1165–H1170.

Berlin, J. R., J. W. Bassani, and D. M. Bers. 1994. Intrinsic cytosolic calcium buffering properties of single rat cardiac myocytes. *Biophys. J.* 67:1775–1787.

Bers, D. M. 1991. Excitation-Contraction Coupling and Cardiac Contractile Force. Kluwer Academic Publishers, Dordrecht, The Netherlands.

Bers, D. M., and A. Peskoff. 1991. Diffusion around a cardiac calcium channel and the role of surface bound calcium. *Biophys. J.* 59:703–721.

Bett, G. C. L. 1995. A mathematical model of the isolated guinea-pig ventricular myocyte. *Biophys. J.* 68:A81.

Blatter, L. A., and W. G. Wier. 1990. Intracellular diffusion, binding, and compartmentalization of the fluorescent calcium indicators indo-1 and fura-2. *Biophys. J.* 58:1491–1499.

Blumenfeld, H., L. Zablow, and B. Sabatini. 1992. Evaluation of cellular mechanisms for modulation of calcium transients using a mathematical model of fura-2 Ca^{2+} imaging in aplysia sensory neurons. *Biophys. J.* 63:1146–1164.

Cannell, M. B., and D. G. Allen. 1984. Model of calcium movements during activation in the sarcomere of frog skeletal muscles. *Biophys. J.* 45:913–925.

Cannell, M. B., H. Cheng, and W. J. Lederer. 1994. Spatial non-uniformities in $[Ca^{2+}]_i$ during excitation-contraction coupling in cardiac myocytes. *Biophys. J.* 67:1942–1956.

Cannell, M. B., H. Cheng, and W. J. Lederer. 1995. The control of calcium release in heart muscle. *Science.* 268:1045–1049.

Cheng, H., W. J. Lederer, and M. B. Cannell. 1993. Calcium sparks: elementary events underlying excitation-contraction coupling in heart muscle. *Science.* 262:740–743.

Cheng, H., M. R. Lederer, W. J. Lederer, and M. B. Cannell. 1996. Calcium sparks and $[Ca^{2+}]_i$ waves in cardiac myocytes. *Am. J. Physiol.* 270:C148–C159.

Crank, J. 1975. The Mathematics of Diffusion, 2nd ed. Oxford University Press, London.

Forbes, M. S., and E. E. Van Niel. 1988. Membrane systems of guinea pig myocardium: ultrastructure and morphometric studies. *Anat. Rec.* 222: 362–379.

Gasbjerg, P. K., A. Horowitz, R. A. Tuft, W. A. Carrington, F. S. Fay, and K. E. Fogarty. 1994. Analysis of the true 3-dimensional point spread function and its effects on quantitative fluorescence microscopy. *Biophys. J.* 66:A274.

Gear, C. W. 1971. The automatic integration of ordinary differential equations. *Commun. ACM.* 14:176–179.

Hiraoka, Y., J. W. Sedat, and D. A. Agard. 1990. Determination of three-dimensional properties of a light microscope system. *Biophys. J.* 57:325–333.

Hodgkin, A. L., and R. D. Keynes. 1957. Movements of labelled calcium in squid giant axons. *J. Physiol. (London).* 138:253–281.

Holmes, T. J., S. Bhattacharyya, J. A. Cooper, D. Hanzel, V. Krishnamurthi, W. Lin, B. Koysam, D. H. Szarowski, and J. N. Turner. 1995. Light microscopic images reconstructed by maximum likelihood deconvolution. *In* Handbook of Biological Confocal Microscopy. J. B. Pawley, editor. Plenum Publishing Company, New York. 389–402.

Keating, T. J., and R. J. Cork. 1994. Improved spatial resolution in ratio images using computational confocal techniques. *Methods Cell Biol.* 40:221–241.

Klein, M. G., H. Cheng, L. F. Santana, Y. H. Jiang, W. J. Lederer, and M. F. Schneider. 1996. Two mechanisms of quantized calcium release in skeletal muscle. *Nature (London).* 379:455–458.

Klein, M. G., L. Kovacs, B. J. Simon, and M. F. Schneider. 1991. Decline of myoplasmic Ca^{2+}, recovery of calcium release and sarcoplasmic Ca^{2+} pump properties in frog skeletal muscle. *J. Physiol. (London).* 441:639–671.

Lewis-Carl, S., K. Felix, A. H. Caswell, N. R. Brandt, W. J. Ball, Jr., P. L. Vaghy, G. Meissner, and D. G. Ferguson. 1995. Immunolocalization of sarcolemmal dihydropyridine receptor and sarcoplasmic reticular triadin and ryanodine receptor in rabbit ventricle and atrium. *J. Cell Biol.* 129:673–682.

Lipp, P., and E. Niggli. 1994. Modulation of Ca^{2+} release in cardiac myocytes: insight from subcellular release patterns revealed by confocal microscopy. *Circ. Res.* 74:979–990.

López-López, J. R., P. S. Shacklock, C. W. Balke, and W. G. Wier. 1994. Local, stochastic release of Ca^{2+} in voltage-clamped rat heart cells: visualization with confocal microscopy. *J. Physiol. (London).* 480: 21–29.

López-López, J. R., P. S. Shacklock, C. W. Balke, and W. G. Wier. 1995. Local calcium transients triggered by single L-type calcium channel currents in cardiac cells. *Science.* 268:1042–1045.

Mattiazi A., L. Hove-Madsen, and D. M. Bers. 1994. Protein kinase inhibitors reduce SR Ca transport in permeabilized myocytes. *Am. J. Physiol.* 267:H812–H820.

Nelson, M. T., H. Cheng, M. Rubart, L. F. Santana, A. D. Bonev, H. J. Knot, and W. J. Lederer. 1995. Relaxation of arterial smooth muscle by calcium sparks. *Science.* 270:633–637.

Niggli, E., and P. Lipp. 1995. Subcellular features of calcium signalling in heart muscle: what do we learn? *Cardiovasc. Res.* 29:441–448.

Parker, I., and Y. Yao. 1991. Regenerative release of calcium from functionally discrete subcellular stores by inositol triphosphate. *Proc. R. Soc. Lond.* B 246:269–274.

Parker, I., and W. G. Wier. 1996. Ca^{2+}-sparks studied by stationary point confocal femtofluorimetry. *J. Mol. Cell. Cardiol.* 28:A132

Parker, I., and Y. Yao. 1996. Ca^{2+} transients associated with openings of inositol triphosphate-gated channels in *Xenopus* oocytes. *J. Physiol. (London).* In press.

Pawley, J. 1995. Fundamental limits in confocal microscopy. 1995. *In* Handbook of Biological Confocal Microscopy. J. B. Pawley, editor. Plenum Publishing Company, New York. 19–37.

Pratusevich, V. R., V. S. Zykov, and M. R. Mukumov. 1987. Evaluation of the action of the cardiotropic substances using a mathematical model of excitation-contraction coupling. *Biophysics.* 32:721–726.

Rousseau, E., and G. Meissner. 1989. Single cardiac sarcoplasmic reticulum Ca^{2+} release channel: activation by caffeine. *Am. J. Physiol.* 256: H328–H333.

Russ, J. C. 1995. The Image Processing Handbook, 2nd ed. CRC Press, Boca Raton, FL.

Sandison, D. R., R. M. Williams, K. S. Wells, J. Strickler, and W. W. Webb. 1995. Quantitative fluorescence confocal laser scanning microscopy (CLSM). *In* Handbook of Biological Confocal Microscopy. J. B. Pawley, editor. Plenum Publishing Company, New York. 39–53.

Shacklock, P. S., W. G. Wier, and C. W. Balke. 1995. Local Ca^{2+} transients (Ca^{2+}-sparks) originate at transverse tubules in rat heart cells. *J. Physiol. (London).* 487:601–608.

Shaw, P. J. 1995. Comparison of wide-field/deconvolution and confocal microscopy for 3D imaging. *In* Handbook of Biological Confocal Microscopy. J. B. Pawley, editor. Plenum Publishing Company, New York. 373–387.

Sheppard, C. J. R., X. Gan, M. Gu, and M. Roy. 1995. Signal-to-noise ratio in confocal microscopes. *In* Handbook of Biological Confocal Microscopy. J. B. Pawley, editor. Plenum Publishing Company, New York. 363–371.

Sipido, K. R., and W. G. Wier. 1991. Flux of Ca^{2+} across the sarcoplasmic reticulum of guinea-pig cardiac cells during excitation-contraction coupling. *J. Physiol. (London).* 435:605–630.

Stern, M. D. 1992. Theory of excitation-contraction coupling in cardiac muscle. *Biophys. J.* 63:497–517.

Tinker, A., A. R. Lindsay, and A. J. Williams. 1992. A model for ionic conduction in the ryanodine receptor channel of sheep cardiac muscle sarcoplasmic reticulum. *J. Gen. Physiol.* 100:495–517.

Tsugorka, A., E. Rios, and L. A. Blatter. 1995. Imaging elementary events of calcium release in skeletal muscle cells. *Science.* 269:1723–1726.

Wagner, J., and J. Keizer. 1994. Effects of rapid buffers on Ca^{2+} diffusion and Ca^{2+} oscillations. *Biophys. J.* 67:447–456.

Wier, W. G. 1992. $[Ca^{2+}]_i$ transients during excitation-contraction coupling of mammalian heart. *In* The Heart and Cardiovascular System, 2nd ed. H. A. Fozzard, editor. Raven Press, New York. 1223–1248.

Wier, W. G., and D. T. Yue. 1986. Intracellular calcium transients underlying the short term force-interval relationship in ferret myocardium. *J. Physiol. (London.)* 376:507–530.

Wimsatt, D. K., C. M. Hohl, G. P. Brierley, and R. A. Altschuld. 1990. Calcium accumulation and release by the sarcoplasmic reticulum of digitonin-lysed adult mammalian ventricular cardiomyocytes. *J. Biol. Chem.* 265:14849–14857.

Zador, A., C. Koch, and T. H. Brown. 1990. Biophysical model of a Hebbian synapse. *Proc. Natl. Acad. Sci. USA.* 87:6718–6722.